



OPEN

Fabrication and characterization of up-converting β - $\text{NaYF}_4:\text{Er}^{3+}, \text{Yb}^{3+} @ \text{NaYF}_4$ core-shell nanoparticles for temperature sensing applications

Lam Thi Kieu Giang^{1,2}✉, Karolina Trejgis³, Lukasz Marciniak³, Nguyen Vu¹ & Le Quoc Minh^{1,4}

This paper presents the use of soft template method to synthesize core and core-shell up-converting nanoparticles useful for temperature sensing applications. Based on the stock solutions of core β - $\text{NaYF}_4:\text{Er}^{3+}, \text{Yb}^{3+}$ nanoparticles and involving soft template method without any additional process of surface functionalization, it is possible to directly design the core-shell β - $\text{NaYF}_4:\text{Er}^{3+}, \text{Yb}^{3+} @ \text{NaYF}_4$ nanoparticles, which can be perfectly dispersed in cyclohexane and surfactants like oleic acid (OA), triethanolamine (TEA) or Cetyltrimethylammonium bromide (CTAB). The morphological, crystalline and elemental characteristics of samples were investigated by Field Emission Scanning Electron Microscopy, X-Ray Diffraction, High Resolution Transmission Electron Microscopy, Selected Area Electron Diffraction patterns and Energy-Dispersive X-Ray Spectroscopy (EDX) measurements. The results showed that the synthesized $\text{NaYF}_4:\text{Er}^{3+}, \text{Yb}^{3+} @ \text{NaYF}_4$ core-shell nanoparticles have roughly spherical shape, pure hexagonal β phase with core size of about 35 ± 5 nm and shell thickness of about 40 ± 5 nm. It has been shown that the coating of the β - $\text{NaYF}_4:\text{Er}^{3+}, \text{Yb}^{3+}$ core with NaYF_4 shell layer enables to enhance the green upconversion (UC) emission intensities in respect to red one. Under 976 nm excitation, the synthesized β - $\text{NaYF}_4:2\%\text{Er}^{3+}, 19\%\text{Yb}^{3+} @ \text{NaYF}_4$ core-shell nanoparticles revealed three strong emission bands at 520 nm, 545 nm and 650 nm corresponding to ${}^2\text{H}_{11/2}$, ${}^4\text{S}_{3/2}$ and ${}^4\text{F}_{9/2}$ to ${}^4\text{I}_{15/2}$ transitions of Er^{3+} ions with the lifetimes of 215, 193 and 474 μs , respectively. The calculated CIE chromaticity coordinates proved that the emission colour of core-shell nanoparticles was changed from red into yellowish green upon increasing the power density of the 976 nm laser from 0.73 to 9.95 W/cm^2 . The calculated slopes indicated that in the β - $\text{NaYF}_4:2\%\text{Er}^{3+}, 19\%\text{Yb}^{3+} @ \text{NaYF}_4$ core-shell nanoparticles, two-photon and three-photon UC processes took place simultaneously. Although the former one is similar as in the case of β - $\text{NaYF}_4:\text{Er}^{3+}, \text{Yb}^{3+}$ bare core nanoparticles, the latter one, three-photon UC process for green emission occurs, due to cross relaxation processes of two Er^{3+} ions only within nanoparticles with core-shell architecture. Moreover, the energy difference between the ${}^2\text{H}_{11/2}$ and ${}^4\text{S}_{3/2}$ levels and associated constant of $\text{NaYF}_4 @ \text{NaYF}_4$ host lattice were determined and they reached $\sim 813 \text{ cm}^{-1}$ and 14.27 ($r^2 = 0.998$), respectively. In order to investigate the suitability of nanoparticles for optical temperature sensing, the emission spectra were measured in a wide temperature range from 158 to 298 K. An exceptionally high value of relative sensitivity was obtained at 158 K and it amounted to $4.25\% \text{ K}^{-1}$. Further temperature increase resulted in gradual

¹Institute of Materials Science, Vietnam Academy of Science and Technology, 18 Hoang Quoc Viet Road, Cau Giay District, Hanoi, Vietnam. ²Graduate University of Science and Technology, Vietnam Academy of Science and Technology, 18 Hoang Quoc Viet Road, Cau Giay District, Hanoi, Vietnam. ³Institute of Low Temperature and Structural Research, Polish Academy of Sciences, ul. Okólna 2, 50-422 Wrocław, Poland. ⁴Duy Tan University, 7/25 Quang Trung, Da Nang, Vietnam. ✉email: giangltk@ims.vast.ac.vn

decrease of relative sensitivity, however, it maintained a high value $> 1\% \text{ K}^{-1}$ in the entire analyzed temperature range.

Temperature is an important physical parameter which governs many fields of science, such as medicine, biology, microelectronics, physics, and chemistry¹. Therefore, many methods of temperature measurements, both contact and non-contact, have been developed based on the mechanical, electrical or optical characteristics^{2–4}. However, to determine the temperature of small, moving or inaccessible objects, the non-contact luminescent thermometry which exploits thermal changes of spectral or temporal properties of the phosphor attached to the object is a preferred technique^{4,5}. One of the most extensively investigated group of lanthanide-based luminescent thermometers are those which for temperature sensing, take advantage of thermally coupled energy levels, like in the case of Er^{3+} , Tm^{3+} , Ho^{3+} , Pr^{3+} or $\text{Eu}^{3+6–10}$. In recent years, the upconversion luminescence of rare-earth ions (RE^{3+}) doped fluoride nanomaterials has received much attention due to their potential applications in various fields such as bioimaging, biolabeling, photodynamic therapy, as drug carriers, optical temperature sensors, etc.^{11–18}. In the case of the optical temperature sensing applications, researchers focused especially on the sodium yttrium fluoride nanoparticles doped or co-doped with rare earth ions ($\text{NaYF}_4:\text{RE}^{3+}$ nanoparticles)^{19–24}, among which the $\text{NaYF}_4:\text{Er}^{3+}, \text{Yb}^{3+}$ nanoparticles were regarded as one of the most efficient upconversion materials for temperature sensing due to their unique luminescence properties and the large energy gap between two thermally coupled $^2\text{H}_{1/2}$ and $^4\text{S}_{3/2}$ energy levels^{25–27}. One of the most important parameter of temperature sensor is its relative sensitivity to temperature changes which verify its quality as well as range of their applications. The improvement of the thermometer sensitivity can be influenced by many factors, e.g. the effect of the phase of $\beta\text{-NaYF}_4:\text{Er}^{3+}, \text{Yb}^{3+}$ and $\alpha\text{-NaYF}_4:\text{Er}^{3+}, \text{Yb}^{3+}$ nanoparticles on the relative sensitivity has been compared. Under the same experimental conditions, i.e. under 980 nm excitation and in a wide temperature range from 328 to 550 K, the $\beta\text{-NaYF}_4:\text{Er}^{3+}, \text{Yb}^{3+}$ nanoparticles revealed significantly higher sensitivities of $0.42\% \text{ K}^{-1}$ and $0.466\% \text{ K}^{-1}$ at 328 K and 550 K²⁶, respectively than α -phase counterpart²⁷. This confirms the importance of conscious synthesis process for the intentional obtaining of highly temperature sensitive nanomaterials and explains the reason for using beta phase nanomaterials in our research.

In our previous research the upconversion (UC) emission properties of uncoated $\beta\text{-NaYF}_4:\text{Er}^{3+}, \text{Yb}^{3+}$ nanoparticles under 976 nm excitation have been investigated. In that case, emission spectra consisted mainly of red emission band at 650 nm, while the green part of spectrum covering the bands at 520 nm and 545 nm was very weak²⁸. In order to enhance the green emission intensities used for temperature sensing applications, in this study a $\beta\text{-NaYF}_4:\text{Er}^{3+}, \text{Yb}^{3+}$ nanoparticles coated with NaYF_4 shell layer are presented. These core-shell nanoparticles were synthesized through the slightly modified soft template method reported previously²⁸. The detailed comparison of UC emission properties under 976 nm excitation with power density changed from 0.73 to 9.95 W/cm^2 , the lifetimes and CIE chromaticity coordinates as well as emission mechanisms of uncoated $\beta\text{-NaYF}_4:\text{Er}^{3+}, \text{Yb}^{3+}$ nanoparticles and $\text{NaYF}_4:\text{Er}^{3+}, \text{Yb}^{3+}@\text{NaYF}_4$ core-shell nanoparticles was also made. Moreover, the luminescence intensity ratio (LIR) of thermally coupled $^2\text{H}_{1/2}$ and $^4\text{S}_{3/2}$ excited states as a function of temperature ranging from 158 to 320 K was investigated. Based on the values of LIR, both the absolute and relative thermal sensitivities were determined. The maximal value of relative sensitivity reached $4.25\% \text{ K}^{-1}$ (at 158 K), confirming great suitability of these $\text{NaYF}_4:\text{Er}^{3+}, \text{Yb}^{3+}@\text{NaYF}_4$ core-shell nanoparticles for optical thermometry.

Experimental

Materials. The rare earth acetate hydrate salt precursors ($\text{RE}(\text{CH}_3\text{COO})_3 \cdot x\text{H}_2\text{O}$, 99.9%) including yttrium (III) acetate hydrate ($\text{Y}(\text{CH}_3\text{COO})_3 \cdot x\text{H}_2\text{O}$, 99.9%), ytterbium(III) acetate hydrate ($\text{Yb}(\text{CH}_3\text{COO})_3 \cdot x\text{H}_2\text{O}$, 99.9%), erbium(III) acetate hydrate ($\text{Er}(\text{CH}_3\text{COO})_3 \cdot x\text{H}_2\text{O}$, 99.9%) were purchased from Sigma-Aldrich. The oleic acid (OA , $\text{CH}_3(\text{CH}_2)_7\text{CH}=\text{CH}(\text{CH}_2)_7\text{COOH}$, 99%), ammonium fluoride (NH_4F , 98%), sodium acetate (CH_3COONa , 99%), isopropanol (IPA, $(\text{CH}_3)_2\text{CHOH}$, 99%), cyclohexane (C_6H_{12} , 99%) and methanol (CH_3OH , 99%) were purchased from Merck.

Synthesis methods. The $\beta\text{-NaYF}_4$ co-doped with 2% mol of Er^{3+} and 19% mol of Yb^{3+} core nanoparticles ($\beta\text{-NaYF}_4:\text{Er}^{3+}, \text{Yb}^{3+}$ CNP) and $\beta\text{-NaYF}_4@\text{NaYF}_4$ co-doped 2% mol of Er^{3+} and 19% mol of Yb^{3+} core-shell nanoparticles ($\beta\text{-NaYF}_4:\text{Er}^{3+}, \text{Yb}^{3+}@\text{NaYF}_4$ CSNP) were prepared by soft-template method as shown in Fig. 1.

Synthesis of $\beta\text{-NaYF}_4:\text{Er}^{3+}, \text{Yb}^{3+}$ CNP. The $\beta\text{-NaYF}_4:\text{Er}^{3+}, \text{Yb}^{3+}$ CNP were prepared via the slightly modified soft template method reported previously²⁸. Yttrium acetate hydrate (0.79 mmol), erbium acetate hydrate (0.02 mmol) and ytterbium acetate tetrahydrate (0.19 mmol) were dispersed in 50 ml solution containing 10 ml IPA and 15 ml OA by ultrasonic cleaner for 30 min. To form a homogeneous solution, the mixture were stirred at 60°C for 60 min under argon atmosphere. Then the mixed solution containing 1.1 mmol sodium acetate, 4.0 mmol ammonium fluoride and 10 ml of methanol was slowly added to the solution under magnetic stirring for another 30 min. Finally, the reaction mixture was heated up to 160°C and stirred for 2 h under argon atmosphere, then cooled down to room temperature in the ice water bath to obtain the stock solution of $\beta\text{-NaYF}_4:\text{Er}^{3+}, \text{Yb}^{3+}$ CNP.

Preparation of the shell precursor solution of NaYF_4 . The shell precursor solution of NaYF_4 was prepared analogously to the $\beta\text{-NaYF}_4:\text{Er}^{3+}, \text{Yb}^{3+}$ CNP as described above however using 1.0 mmol yttrium acetate hydrate, without addition of erbium and ytterbium acetates.

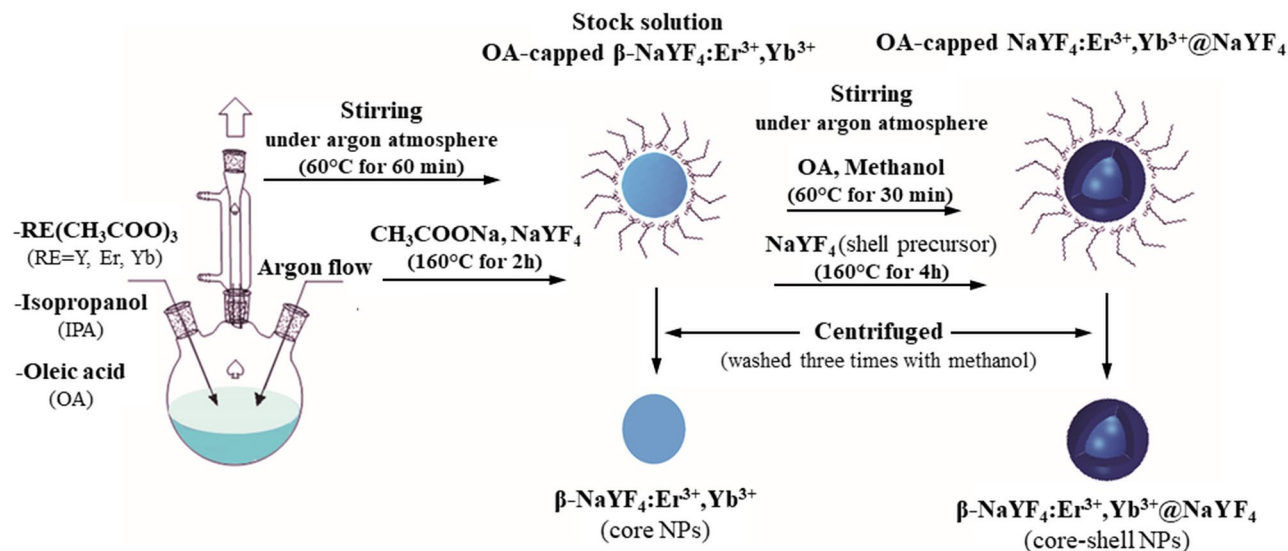


Figure 1. Schematic diagram of preparation of $\beta\text{-NaYF}_4\text{:Er}^{3+},\text{Yb}^{3+}$ CNP and $\beta\text{-NaYF}_4\text{:Er}^{3+},\text{Yb}^{3+}@NaYF_4$ CSNP using soft-template method.

Synthesis of $\beta\text{-NaYF}_4\text{:Er}^{3+},\text{Yb}^{3+}@NaYF_4$ CSNP. Dispersion of 30 ml stock solution of prepared $\beta\text{-NaYF}_4\text{:Er}^{3+},\text{Yb}^{3+}$ CNP (described above) in mixed solution of 10 ml oleic acid and 15 ml methanol was carried out using ultrasonic bath for 30 min. Then, the homogeneous mixture of $\beta\text{-NaYF}_4\text{:Er}^{3+},\text{Yb}^{3+}$ CNP with oleate ligands capping the surface was achieved via stirring at 60 °C for 30 min under argon atmosphere. Finally, during another 30 min lasting stirring at 60 °C under argon atmosphere the 30 ml of the shell precursor solution of NaYF_4 was slowly added to the mixture and then heated up to 160 °C for 4 h, then cooled down to room temperature in the ice water bath to obtain the solution of $\beta\text{-NaYF}_4\text{:Er}^{3+},\text{Yb}^{3+}@NaYF_4$ CSNP.

The precipitated $\beta\text{-NaYF}_4\text{:Er}^{3+},\text{Yb}^{3+}$ CNP and $\beta\text{-NaYF}_4\text{:Er}^{3+},\text{Yb}^{3+}@NaYF_4$ CSNP were centrifuged and washed three times with methanol, then dried at 60 °C and dispersed in cyclohexane.

Characterization. The morphology of synthesized $\beta\text{-NaYF}_4\text{:Er}^{3+},\text{Yb}^{3+}$ CNP and $\beta\text{-NaYF}_4\text{:Er}^{3+},\text{Yb}^{3+}@NaYF_4$ CSNP were carried out by Field Emission Scanning Electron Microscope (FESEM, Hitachi S-4800). Transmission Electron Microscopy images were recorded using Tecnai 20 D2094 X-Twin Microscope operating at 200 kV, in which, the samples were prepared by dispersion in ethanol with an ultrasonic bath for 20 min, then put on the copper grids. Selected Area Electron Diffraction (SAED) patterns and Energy Dispersive X-ray Spectroscopy (EDX) elementals mapping were carried out using Tecnai 20 D2094 X-Twin Microscope operating at 200 kV. Structural analysis of samples was determined by X-Ray Diffraction (PANalytical X'Pert Pro Powder Diffractometer) using $\text{Cu K}\alpha$ radiation ($\lambda = 1.54060 \text{ \AA}$) in the 2θ range from 10° to 80° .

The Fourier Transform Infrared Spectroscopy (FTIR) analysis was recorded using a Thermo Nicolet NEXUS 670 FTIR (USA) in a KBr suspension in the region of 4000 to 400 cm^{-1} .

The upconversion emission spectra were measured with a Jobin-Yvon HR1000 monochromator, equipped with a charge-coupled device (CCD) camera at temperature in range from 158 to 320 K by the use of THMS600 heating-cooling stage from Linkam and using a 976 nm laser diode of power density changed in a range from 0.73 to 9.95 W/cm^2 . The upconversion luminescence decay curves were measured with a LeCroy WaveSurfer 400 oscilloscope.

Results and discussion

Comparison of morphological and structural properties of the uncoated nanoparticles ($\text{NaYF}_4\text{:Er}^{3+},\text{Yb}^{3+}$ CNP) and core-shell structures ($\text{NaYF}_4\text{:Er}^{3+},\text{Yb}^{3+}@NaYF_4$ CSNP) is shown in Figs. 2, 3 and 4. As can be seen in the FESEM image (Fig. 2a), the synthesized $\text{NaYF}_4\text{:Er}^{3+},\text{Yb}^{3+}$ CNP were roughly spherical in shape with sizes of around $35 \pm 5 \text{ nm}$. The HR-TEM image in Fig. 2b presents a representative nanoparticle with size of 36 nm and lattice distance of 0.3 nm corresponding to d-spacing for the (110) lattice plane of hexagonal β phase of NaYF_4 structures, suggesting that the [110] is the preferred growth direction of the $\text{NaYF}_4\text{:Er}^{3+},\text{Yb}^{3+}$ CNP. The clear difference between core and shell part of the nanoparticle observed in TEM images may results from the difference in the porosity of the particular parts of the nanocrystal. In addition, the obtained SEAD pattern in Fig. 2c indicates the diffraction rings which correspond to the (100), (110), (101), (200), (111), (201), (210) and (300) planes of the synthesized $\beta\text{-NaYF}_4$ nanoparticles. The EDX spectrum analysis shows the major peaks at energy around 0.68 , 1.04 , 1.91 and 8.04 keV corresponding to F, Na, Y of synthesized $\text{NaYF}_4\text{:Er}^{3+},\text{Yb}^{3+}$ CNP and Cu elements of copper grid (Fig. 2d). The minor intensity peaks observed at energy around 1.54 , 7.39 , 8.42 , 14.9 and 16.73 keV have proven the presence of Yb^{3+} and Y^{3+} ions in the samples. The presence of Er^{3+} ions at energy around 6.9 keV is almost invisible which is due to the low concentration of Er^{3+} ions in the material.

The characteristic properties of $\text{NaYF}_4\text{:Er}^{3+},\text{Yb}^{3+}@NaYF_4$ CSNP are presented in Fig. 3. As can be observed in Fig. 3a–c, after coating the surface of $\text{NaYF}_4\text{:Er}^{3+},\text{Yb}^{3+}$ CNP with a shell layer of NaYF_4 , the synthesized

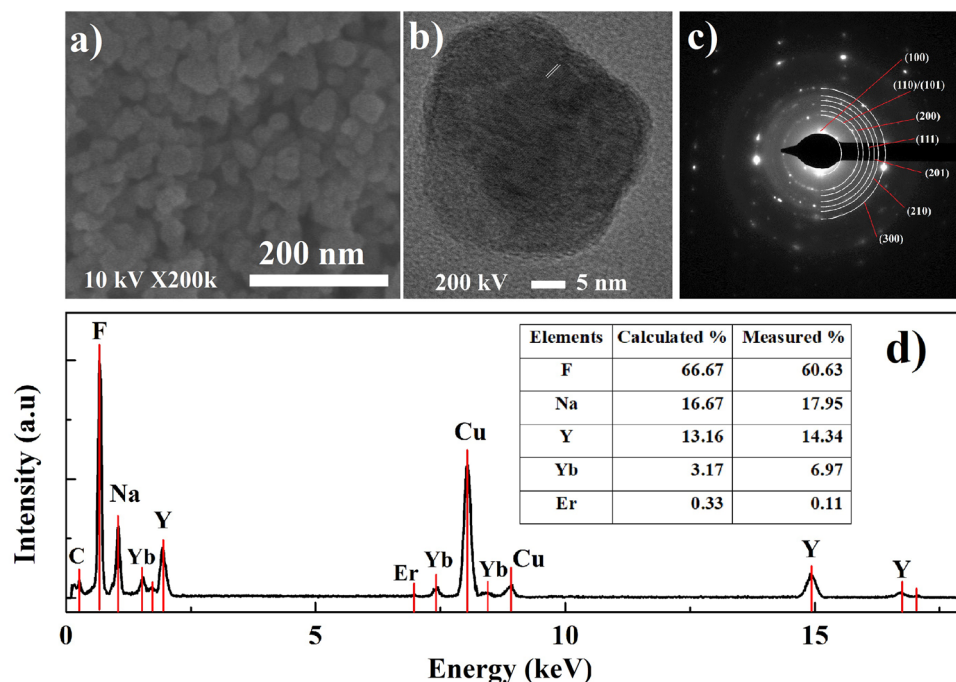


Figure 2. Characterization of synthesized $\text{NaYF}_4:\text{Er}^{3+}, \text{Yb}^{3+}$ CNP: (a) FESEM and (b) HR-TEM images, (c) SAED pattern and (d) EDX spectrum corresponding to the isometric nanoparticles in (c).

$\text{NaYF}_4:\text{Er}^{3+}, \text{Yb}^{3+}@ \text{NaYF}_4$ samples revealed also roughly spherical shape however, with obviously larger average size than that of the above-mentioned $\text{NaYF}_4:\text{Er}^{3+}, \text{Yb}^{3+}$ CNP precursors. The diameter of the core-shell nanoparticles was on average 100 ± 10 nm. It can be clearly seen that the NaYF_4 shell layer with thickness about 40 nm covered the entire surface of $\text{NaYF}_4:\text{Er}^{3+}, \text{Yb}^{3+}$ CNP, indicating the formation of core-shell structure in the synthesized $\text{NaYF}_4:\text{Er}^{3+}, \text{Yb}^{3+}@ \text{NaYF}_4$ CSNP. In particular, the HR-TEM image (Fig. 3d) has shown that the lattice distances were equal to 0.3 nm as in the case of uncovered NPs and 0.5 nm corresponding to d-spacing for the (110) and (100) lattice planes of $\beta\text{-NaYF}_4$ nanoparticles. It suggests that the [110] growth direction is preferred both in the case of uncovered $\text{NaYF}_4:\text{Er}^{3+}, \text{Yb}^{3+}$ CNP as well as in the case of core-shell $\text{NaYF}_4:\text{Er}^{3+}, \text{Yb}^{3+}@ \text{NaYF}_4$ CSNP. Figure 3e displays the diffraction rings corresponding to the (100), (110), (101), (200), (111), (201), (210) and (220) planes of the $\beta\text{-NaYF}_4$ nanoparticles thus confirming the formation of hexagonal β phase of synthesized $\text{NaYF}_4:\text{Er}^{3+}, \text{Yb}^{3+}@ \text{NaYF}_4$ CSNP. Furthermore, the results of EDX spectrum analysis confirmed the presence of F, Na, Y host elements which were related to the major peaks at energy around 0.67, 1.04, 1.92 and 8.04 keV (Fig. 3f). However, the intensities of peaks corresponding to Yb element at energy around 1.54, 7.39 and 8.42 keV in the $\text{NaYF}_4:\text{Er}^{3+}, \text{Yb}^{3+}@ \text{NaYF}_4$ CSNP were much lower compared with the $\text{NaYF}_4:\text{Er}^{3+}, \text{Yb}^{3+}$ CNP, suggesting as expected a decrease of $\text{Yb}^{3+}/\text{NaYF}_4$ ratio in the $\text{NaYF}_4:\text{Er}^{3+}, \text{Yb}^{3+}@ \text{NaYF}_4$ CSNP since the ratio of Yb^{3+} ions to the total amount of ions is lower in the case of CSNP in respect to the CNP counterpart due to the additional shell layer with no Yb^{3+} ions. The presence of Er^{3+} ions was not observed in the $\text{NaYF}_4:\text{Er}^{3+}, \text{Yb}^{3+}@ \text{NaYF}_4$ CSNP due to the Er^{3+} concentration below the detection limit of the measurement.

The normalized XRD patterns of $\text{NaYF}_4:\text{Er}^{3+}, \text{Yb}^{3+}$ CNP and $\text{NaYF}_4:\text{Er}^{3+}, \text{Yb}^{3+}@ \text{NaYF}_4$ CSNP are shown in Fig. 4. The diffraction peaks of samples perfectly matched with the standard reference pattern of hexagonal β phase of NaYF_4 (JCPDS card, No. 028-1192) which confirmed the high purity and crystallization of synthesized $\text{NaYF}_4:\text{Er}^{3+}, \text{Yb}^{3+}$ CNP and $\text{NaYF}_4:\text{Er}^{3+}, \text{Yb}^{3+}@ \text{NaYF}_4$ CSNP.

The average crystallite size D of samples was calculated using Scherrer formula²⁹:

$$D = \frac{k\lambda}{\beta \cos \theta} \quad (1)$$

where λ is the X-ray wavelength, β is the full width at half maximum, θ is the diffraction angle and k is a constant. The determined D values were equal 36 nm and 85 nm for $\text{NaYF}_4:\text{Er}^{3+}, \text{Yb}^{3+}$ CNP (pattern a) and $\beta\text{-NaYF}_4:\text{Er}^{3+}, \text{Yb}^{3+}@ \text{NaYF}_4$ CSNP (pattern b), respectively²⁹. The results were entirely consistent with the SEM and TEM images presented above in Figs. 2 and 3.

The ligand binding on the surface of $\beta\text{-NaYF}_4:\text{Er}^{3+}, \text{Yb}^{3+}$ CNP and $\beta\text{-NaYF}_4:\text{Er}^{3+}, \text{Yb}^{3+}@ \text{NaYF}_4$ CSNP were investigated by FTIR spectrum in the wavenumber range from 4000 to 400 cm^{-1} (Fig. 5). As can be seen, in both core and core-shell samples, a broad absorption peak of the O-H stretching vibrations due to intermolecular hydrogen bonding at around 3448 cm^{-1} was observed³⁰. The weak absorption peaks at 2929 cm^{-1} , 2647 cm^{-1} corresponding to the asymmetric and symmetric stretching vibrations of the long alkyl chains ($=\text{CH}(\text{CH}_2)_n$ groups) of oleic acid can be observed confirming its residual presence on the surface of $\beta\text{-NaYF}_4:\text{Er}^{3+}, \text{Yb}^{3+}$ CNP and $\beta\text{-NaYF}_4:\text{Er}^{3+}, \text{Yb}^{3+}@ \text{NaYF}_4$ CSNP. The broad bands at about 1635 cm^{-1} and 1122 cm^{-1} have been assigned

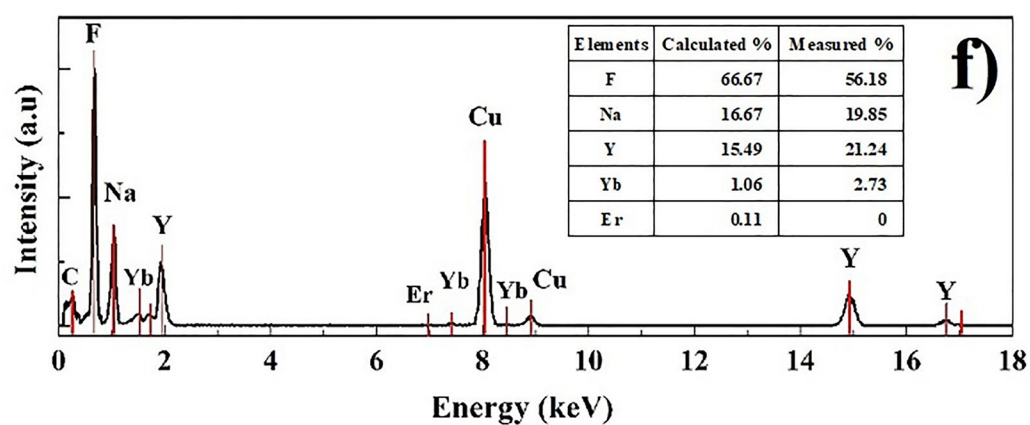
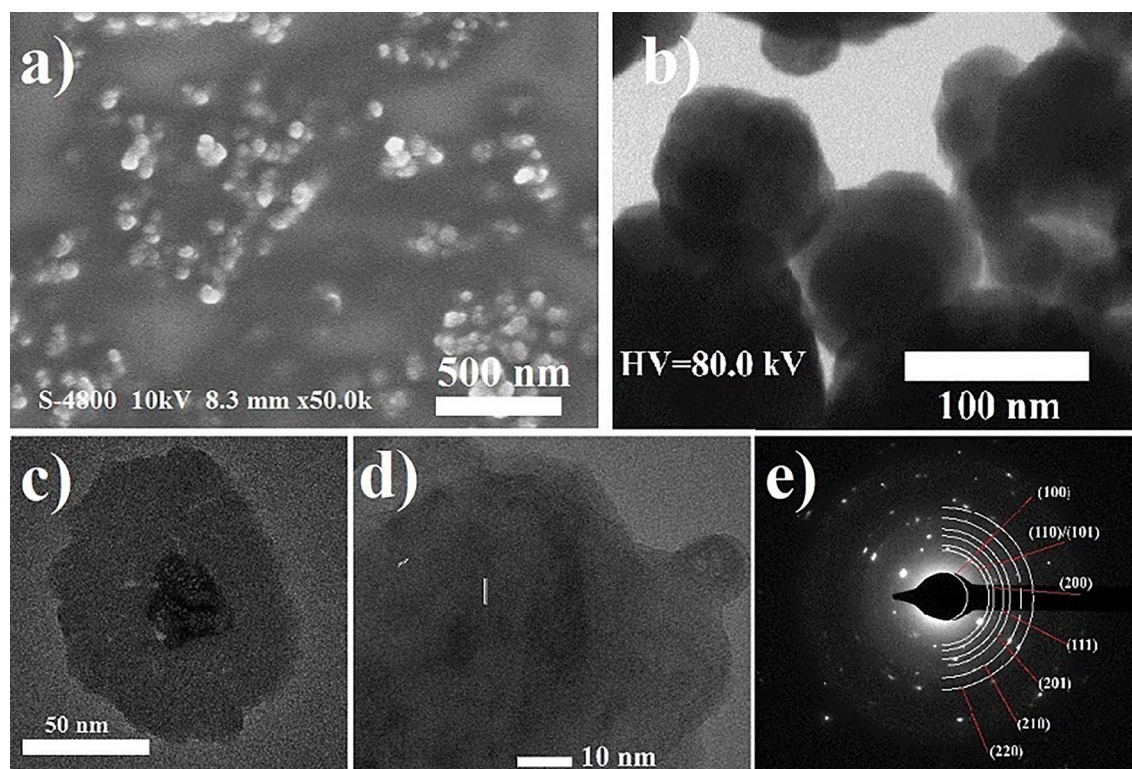


Figure 3. Characterization of $\text{NaYF}_4:\text{Er}^{3+}, \text{Yb}^{3+}@\text{NaYF}_4$ CSNP: (a) FE-SEM, (b) TEM, (c, d) HR-TEM images, (e) SAED pattern and (f) EDX spectrum corresponding to the isometric nanoparticles (e).

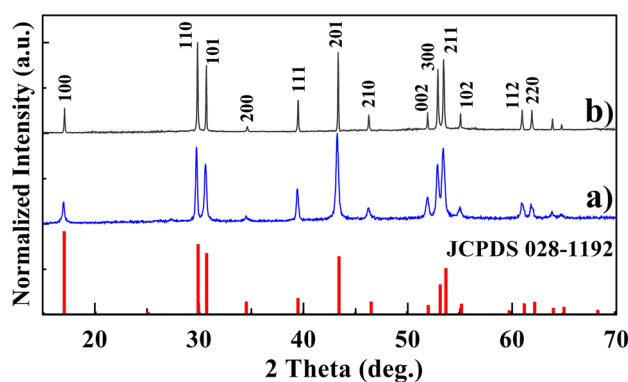


Figure 4. The normalized XRD patterns of synthesized $\text{NaYF}_4:\text{Er}^{3+}, \text{Yb}^{3+}$ CNP (a) and $\text{NaYF}_4:\text{Er}^{3+}, \text{Yb}^{3+}@\text{NaYF}_4$ CSNP (b) compared to standard data of hexagonal β - NaYF_4 phase (JCPDS card No. 028-1192).

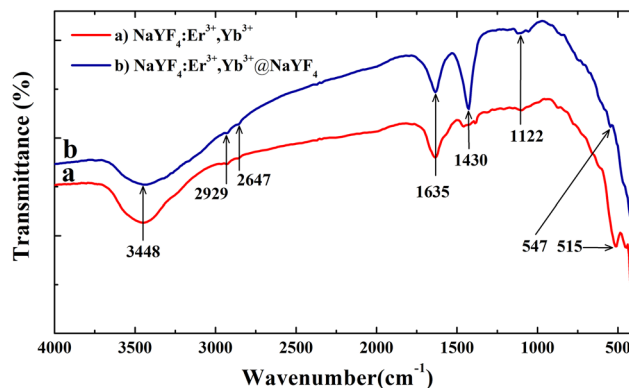


Figure 5. The FTIR spectra of: (a) β - $\text{NaYF}_4:\text{Er}^{3+},\text{Yb}^{3+}$ CNP and (b) β - $\text{NaYF}_4:\text{Er}^{3+},\text{Yb}^{3+}@\text{NaYF}_4$ CSNP in the wavenumber range of 4000 to 400 cm^{-1} .

to the presence of asymmetric and symmetric C=O stretching vibration of carboxylic acid salts on the surface of β - $\text{NaYF}_4:\text{Er}^{3+},\text{Yb}^{3+}$ CNP and β - $\text{NaYF}_4:\text{Er}^{3+},\text{Yb}^{3+}@\text{NaYF}_4$ CSNP³¹ and the peaks at 547 cm^{-1} and 515 cm^{-1} might be a result of a presence of the $\text{RE}^{3+}\text{-F}$ stretching vibrations. Exceptionally, a strong band at 1430 cm^{-1} related to O-H bending vibration of carboxyl group was observed only in the β - $\text{NaYF}_4:\text{Er}^{3+},\text{Yb}^{3+}@\text{NaYF}_4$ CSNP^{17,30}. Therefore, the presence of carboxylic acid groups in the synthesized β - $\text{NaYF}_4:\text{Er}^{3+},\text{Yb}^{3+}@\text{NaYF}_4$ CSNP is suspected³⁰.

In order to study the impact of Er^{3+} and Yb^{3+} ions as well as the energy transfer mechanisms in synthesized β - $\text{NaYF}_4:\text{Er}^{3+},\text{Yb}^{3+}$ CNP and β - $\text{NaYF}_4:\text{Er}^{3+},\text{Yb}^{3+}@\text{NaYF}_4$ CSNP on their spectroscopic properties, the dependence of UC luminescence intensity on the 976 nm excitation (power density changed in the range from 0.73 to 9.95 W/cm^2) have been measured at room temperature. As it is well known, in the low excitation density regime, the UC emission intensity (I), is dependent on the excitation laser power (P) as follows³²:

$$I = AP^n \quad (2)$$

where A is a proportional parameter, n is the number of pumping photons involved in the UC process.

Figure 6 shows the UC emission properties of β - $\text{NaYF}_4:2\%\text{Er}^{3+},19\%\text{Yb}^{3+}$ CNP as a function of pump power of 976 nm laser diode. As can be observed, the β - $\text{NaYF}_4:2\%\text{Er}^{3+},19\%\text{Yb}^{3+}$ CNP revealed strong red emission band at 650 nm corresponding to ${}^4\text{F}_{9/2} \rightarrow {}^4\text{I}_{15/2}$ transition of Er^{3+} ions and minor green emission bands at 520 nm and 545 nm corresponding to ${}^2\text{H}_{11/2}, {}^4\text{S}_{3/2} \rightarrow {}^4\text{I}_{15/2}$ transitions, respectively (Fig. 6a). The UC emission intensity increased with increasing the pump power and the intensity ratio of green to red emission decreased from 0.3 to 0.1 in response to increased excitation power density from 0.73 to 9.95 W/cm^2 . These results suggest that at high excitation densities the red emission is even more dominant. High excitation density provides heating of the nanocrystals, therefore observed changes of green to red emission intensities could be explained in terms of higher probability of nonradiative depopulation of ${}^2\text{H}_{11/2}$ and ${}^4\text{S}_{3/2}$ states to ${}^4\text{F}_{9/2}$ at higher temperatures. The calculated CIE chromaticity coordinates of β - $\text{NaYF}_4:2\%\text{Er}^{3+},19\%\text{Yb}^{3+}$ CNP under 976 nm excitation confirmed that the CIE (x, y) values increased from (0.337, 0.331) to (0.409, 0.356) with the excitation power (Fig. 6b). The obtained CIE (x, y) values proved that the emission color of the β - $\text{NaYF}_4:2\%\text{Er}^{3+},19\%\text{Yb}^{3+}$ CNP can be tuned from yellowish to red by excitation power changes (Table 1). The calculated slopes of the fitting lines of the first 6 points for green (${}^2\text{H}_{11/2}, {}^4\text{S}_{3/2} \rightarrow {}^4\text{I}_{15/2}$) and red (${}^4\text{F}_{9/2} \rightarrow {}^4\text{I}_{15/2}$) emission bands were equal to 1.8 and 1.3, indicating that two photons process was involved to populate excited levels resulting in both green and red emission bands in the synthesized β - $\text{NaYF}_4:2\%\text{Er}^{3+},19\%\text{Yb}^{3+}$ CNP (Fig. 6c).

In addition, luminescence decay curves of ${}^2\text{H}_{11/2}$ (emission band at 520 nm), ${}^4\text{S}_{3/2}$ (emission band at 545 nm) and ${}^4\text{F}_{9/2}$ (emission band at 650 nm) excited levels of β - $\text{NaYF}_4:2\%\text{Er}^{3+},19\%\text{Yb}^{3+}$ CNP and β - $\text{NaYF}_4@\text{NaYF}_4:2\%\text{Er}^{3+},19\%\text{Yb}^{3+}$ CSNP compared with the β - $\text{NaYF}_4:2\%\text{Er}^{3+}$ CNP and β - $\text{NaYF}_4@\text{NaYF}_4:2\%\text{Er}^{3+}$ CSNP under 976 nm excitation were recorded. The average luminescence lifetimes were calculated by the following equation³³:

$$\tau = \frac{\int_0^\infty tI(t)dt}{\int_0^\infty I(t)dt} \quad (3)$$

where $I(t)$ represents the luminescence intensity at time t .

The average decay times of β - $\text{NaYF}_4:2\%\text{Er}^{3+},19\%\text{Yb}^{3+}$ CNP recorded for ${}^2\text{H}_{11/2}$ level (emission band at 520 nm), ${}^4\text{S}_{3/2}$ level (emission at 545 nm) and ${}^4\text{F}_{9/2}$ level (emission at 650 nm) were equal 112, 118 and 512 μs , respectively (Fig. 6e), while for the β - $\text{NaYF}_4:2\%\text{Er}^{3+}$ CNP counterpart they were 19, 18 and 26 μs , respectively (Fig. 6d). The longer lifetimes of Er^{3+} ions in the synthesized β - $\text{NaYF}_4:2\%\text{Er}^{3+},19\%\text{Yb}^{3+}$ CNP compared with the $\text{NaYF}_4:2\%\text{Er}^{3+}$ CNP confirmed the occurrence of effective energy transfer from Yb^{3+} to Er^{3+} ions in β - NaYF_4 host lattice³⁴. What is more, the comparison of the intensities of the bands within the β - $\text{NaYF}_4:2\%\text{Er}^{3+},19\%\text{Yb}^{3+}$ CNP themselves revealed that green emission intensity was much weaker than the red one and associated lifetimes recorded at 520 and 545 nm was about 4.34 times shorter than that recorded at 650 nm.

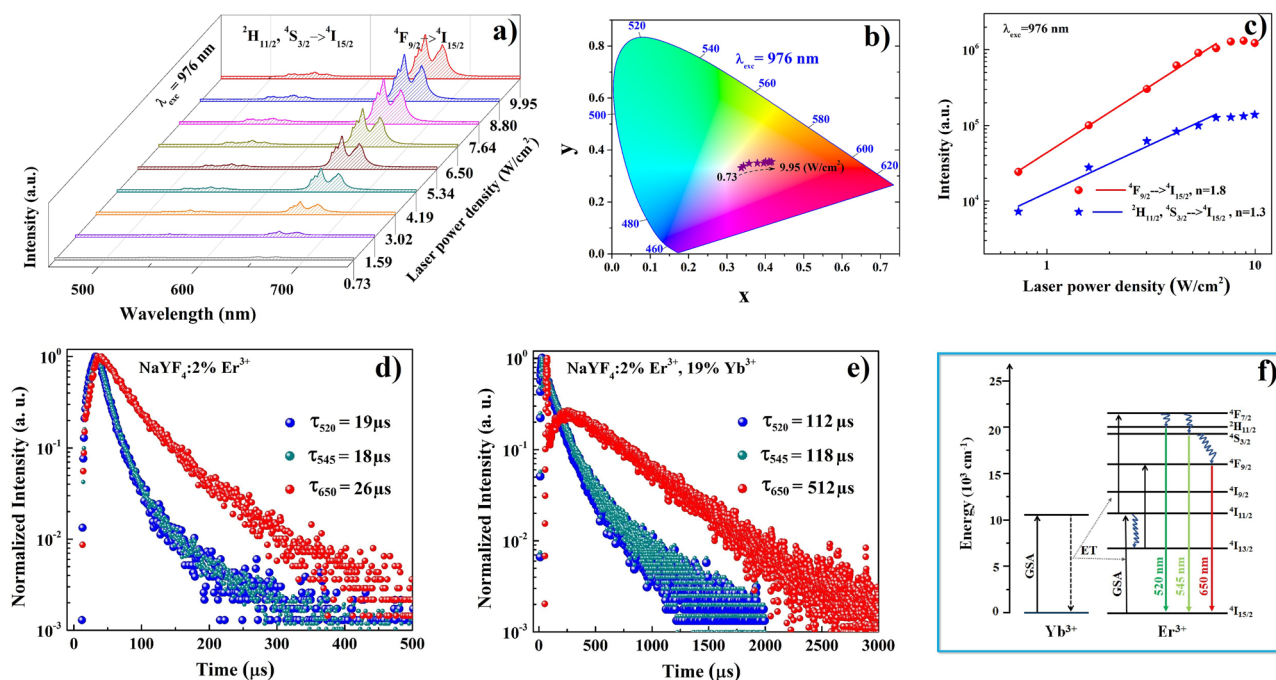
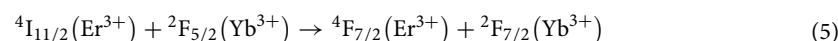
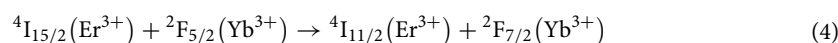


Figure 6. The UC emission spectra (a), CIE1931 chromaticity diagram (b), and integrated intensities (c) of blue (${}^2\text{H}_{11/2}, {}^4\text{S}_{3/2} \rightarrow {}^4\text{I}_{15/2}$) and red (${}^4\text{F}_{9/2} \rightarrow {}^4\text{I}_{15/2}$) emission bands of core $\beta\text{-NaYF}_4:2\%\text{Er}^{3+}, 19\%\text{Yb}^{3+}$ nanoparticles upon 976 nm laser diode excitation in range of 0.73 to 9.95 W/cm^2 . The luminescence decay curves of synthesized $\beta\text{-NaYF}_4:2\%\text{Er}^{3+}$ CNP (d) and $\beta\text{-NaYF}_4:2\%\text{Er}^{3+}, 19\%\text{Yb}^{3+}$ CNP (e) recorded at 520 nm (blue curves), 545 nm (dark cyan curves) and 650 nm (red curves) under 976 nm excitation. The corresponding energy levels diagram of $\text{NaYF}_4:\text{Er}^{3+}, \text{Yb}^{3+}$ nanoparticles (f).

Laser power density (W/cm^2)	Relative integrated intensities			CIE	
	${}^2\text{H}_{11/2}, {}^4\text{S}_{3/2} \rightarrow {}^4\text{I}_{15/2}$	${}^4\text{F}_{9/2} \rightarrow {}^4\text{I}_{15/2}$	$I_{\text{Green}}/I_{\text{Red}}$	x	y
0.73	22.95	77.05	0.30	0.337	0.331
1.59	21.70	78.30	0.28	0.343	0.339
3.02	17.02	82.98	0.21	0.358	0.348
4.19	11.80	88.20	0.13	0.379	0.349
5.34	9.85	90.15	0.11	0.396	0.349
6.50	10.27	89.73	0.11	0.401	0.355
7.64	9.45	90.55	0.10	0.412	0.352
8.80	9.31	90.69	0.10	0.416	0.355
9.95	9.35	90.65	0.10	0.409	0.356

Table 1. The integrated UC intensities of particular emission bands, their ratios and CIE chromaticity coordinates of synthesized $\beta\text{-NaYF}_4:\text{Er}^{3+}, \text{Yb}^{3+}$ CNP.

Basing on the obtained results, the UC mechanism of the $\beta\text{-NaYF}_4:2\%\text{Er}^{3+}, 19\%\text{Yb}^{3+}$ CNP have been proposed as follows: upon a 976 nm laser diode excitation, the activator ions (Er^{3+}) were excited from the ${}^4\text{I}_{15/2}$ ground state to the ${}^4\text{I}_{11/2}$ excited state through ground states absorption (GSA), or energy transfer (ET) from the ${}^2\text{F}_{5/2}$ excited state of Yb^{3+} ions (4). Then, the population of ${}^4\text{I}_{11/2}$ excited state of Er^{3+} ions was followed by excitation to the ${}^4\text{F}_{7/2}$ level due to another energy transfer from Yb^{3+} ions (5).



After the excitation of ${}^4\text{F}_{7/2}$ level of Er^{3+} ions the nonradiative relaxation to the ${}^2\text{H}_{11/2}$ and ${}^4\text{S}_{3/2}$ levels occurred. The radiative depopulation of those levels back to the ground state leads to appearance of green UC emission bands at 520 and 545 nm corresponding to ${}^2\text{H}_{11/2} \rightarrow {}^4\text{I}_{15/2}$ and ${}^4\text{S}_{3/2} \rightarrow {}^4\text{I}_{15/2}$ transitions of Er^{3+} ions, respectively (Fig. 6f)¹⁵. Additionally, the electrons from the ${}^4\text{S}_{3/2}$ level of Er^{3+} ions can be nonradiatively relaxed to the ${}^4\text{F}_{9/2}$

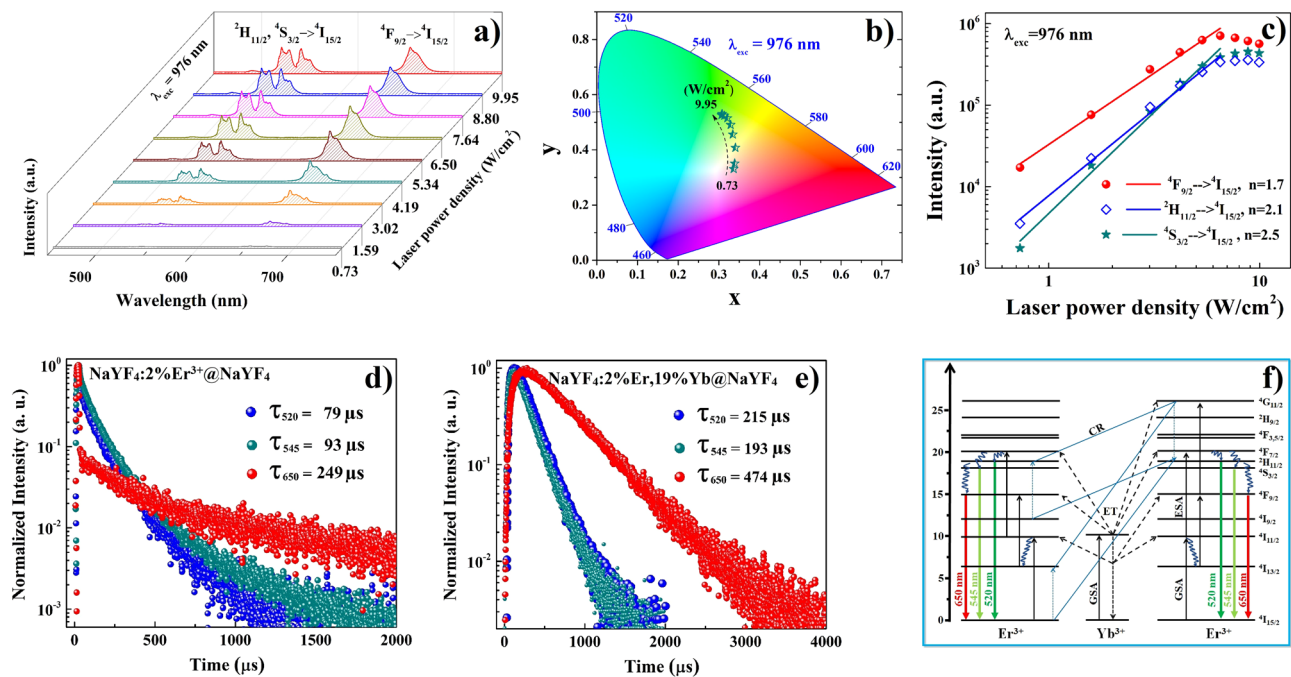


Figure 7. The UC emission spectra (a), and CIE chromaticity diagram (b), and integrated intensities (c) of green (${}^2H_{11/2}$, ${}^4S_{3/2} \rightarrow {}^4I_{15/2}$; dark green- and blue- lines) and red (${}^4F_{9/2} \rightarrow {}^4I_{15/2}$; red-line) emission bands of synthesized $\beta\text{-NaYF}_4:2\%\text{Er}^{3+},19\%\text{Yb}^{3+}@NaYF_4$ CSNP upon 976 nm laser diode excitation in range of 0.73 to 9.95 W/cm^2 . The luminescence decay curves of synthesized $\beta\text{-NaYF}_4:2\%\text{Er}^{3+}@NaYF_4$ (d) and $\beta\text{-NaYF}_4:2\%\text{Er}^{3+},19\%\text{Yb}^{3+}@NaYF_4$ CSNP (e) recorded at 520 nm (blue curves), 545 nm (dark cyan curves) and 650 nm (red curves) under 976 nm excitation. The corresponding energy levels diagram of $\text{NaYF}_4:\text{Er}^{3+},\text{Yb}^{3+}@NaYF_4$ nanoparticles (f).

Laser power density (W/cm^2)	Relative integrated intensities				CIE	
	${}^2H_{11/2} \rightarrow {}^4I_{15/2}$	${}^4S_{3/2} \rightarrow {}^4I_{15/2}$	${}^4F_{9/2} \rightarrow {}^4I_{15/2}$	$I_{\text{Green}}/I_{\text{Red}}$	x	y
0.73	7.83	15.66	76.51	0.31	0.336	0.331
1.59	15.52	19.14	65.34	0.53	0.339	0.351
3.02	18.58	20.97	60.45	0.65	0.341	0.407
4.19	23.33	21.48	55.19	0.81	0.334	0.456
5.34	25.36	21.60	53.04	0.89	0.329	0.490
6.50	26.89	23.61	49.50	1.02	0.321	0.515
7.64	29.67	24.18	46.15	1.17	0.313	0.524
8.80	31.78	25.17	43.06	1.32	0.308	0.530
9.95	32.53	25.12	42.35	1.36	0.306	0.526

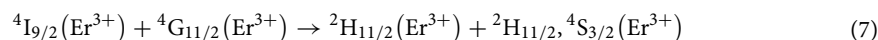
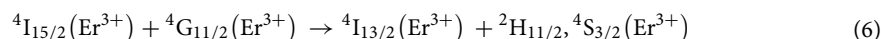
Table 2. The integrated UC intensities of particular emission bands, their ratios and CIE chromaticity coordinates of synthesized $\beta\text{-NaYF}_4:\text{Er}^{3+},\text{Yb}^{3+}@NaYF_4$ CSNP.

level causing the occurrence of the red emission band at 650 nm related to the ${}^4F_{9/2} \rightarrow {}^4I_{15/2}$ electronic transition of Er^{3+} ions. Furthermore, the nonradiative relaxation from ${}^4I_{11/2}$ excited state to the lower ${}^4I_{13/2}$ state of Er^{3+} ions can take place enabling another act of excitation to occur. Therefore, absorption of a second NIR photon can provoke excitation from ${}^4I_{11/2}$ to the ${}^4F_{9/2}$ state³⁴.

In order to study the effect of the shell layer on the UC properties of nanoparticles, an analogous spectroscopic analysis was carried out for $\beta\text{-NaYF}_4:\text{Er}^{3+},\text{Yb}^{3+}@NaYF_4$ CSNP. The UC emission properties of synthesized $\beta\text{-NaYF}_4:\text{Er}^{3+},\text{Yb}^{3+}@NaYF_4$ CSNP upon 976 nm laser diode excitation are presented in Fig. 7. It can be clearly seen that these CSNPs revealed three strong emission bands at 520 nm, 545 nm and 650 nm assigned to ${}^2H_{11/2} \rightarrow {}^4I_{15/2}$, ${}^4S_{3/2} \rightarrow {}^4I_{15/2}$ and ${}^4F_{9/2} \rightarrow {}^4I_{15/2}$ transitions of Er^{3+} ions, respectively (Fig. 7a). The ratio of green to red emission intensities increased from 0.31 to 1.36 with increasing excitation power density from 0.73 to 9.95 W/cm^2 . The calculated CIE chromaticity coordinates of synthesized $\beta\text{-NaYF}_4:2\%\text{Er}^{3+},19\%\text{Yb}^{3+}@NaYF_4$ CSNP proved that the x value decreased from 0.34 to 0.31, while y value increased from 0.33 to 0.53 (Table 2) therefore, the emission colors changed from red into yellowish green (Fig. 7b). The slopes of fitting lines for emission bands associated with the transitions from ${}^4S_{3/2}$ (blue line), ${}^2H_{11/2}$ (wine line) and ${}^4F_{9/2}$ (red line) levels to ${}^4I_{15/2}$ ground state were determined as 2.5, 2.1 and 1.7, respectively (Fig. 7c). These results indicate that in the

case of synthesized $\beta\text{-NaYF}_4\text{:2\%Er}^{3+},19\%\text{Yb}^{3+}\text{@NaYF}_4$ CSNP not only two-photon UC process, as in the above-mentioned $\beta\text{-NaYF}_4\text{:2\%Er}^{3+},19\%\text{Yb}^{3+}$ CNP took place, but also three-photon UC process for green emissions was involved.

The three-photon UC process causing the green emission was observed only in the $\beta\text{-NaYF}_4\text{:2\%Er}^{3+},19\%\text{Yb}^{3+}\text{@NaYF}_4$ CSNP. Therefore it is postulated in this work, that an additional shell layer reduces undesirable surface losses, detain energy within the sample and enable cross-relaxation between Er^{3+} ions to occur. The cross-relaxation processes of two Er^{3+} ions taking place in the way as follows^{34,35}:



To confirm also the energy transfer between Yb^{3+} to Er^{3+} ions in the core-shell $\beta\text{-NaYF}_4\text{@NaYF}_4$ host lattice, the comparison of spectroscopic properties of $\beta\text{-NaYF}_4\text{:2\%Er}^{3+},19\%\text{Yb}^{3+}\text{@NaYF}_4$ CSNP and $\beta\text{-NaYF}_4\text{:2\%Er}^{3+}\text{@NaYF}_4$ CSNP was made. As can be seen in Fig. 7d, the calculated emission lifetimes of single doped $\beta\text{-NaYF}_4\text{:2\%Er}^{3+}\text{@NaYF}_4$ CSNP monitored at 520 nm, 545 nm and 650 nm were 79, 93 and 249 μs , respectively, while in the case of co-doped $\beta\text{-NaYF}_4\text{:2\%Er}^{3+},19\%\text{Yb}^{3+}\text{@NaYF}_4$ CSNP, an approximately three-fold increase in the decay times of green emissions and two-fold of the red one was observed (Fig. 7e) and their values were 215, 193 and 474 μs , respectively. What is more, it can be seen that the lifetime of red emission recorded at 650 nm in the case of synthesized core-shell $\beta\text{-NaYF}_4\text{:2\%Er}^{3+},19\%\text{Yb}^{3+}\text{@NaYF}_4$ CSNP was slightly shorter than in uncoated $\beta\text{-NaYF}_4\text{:2\%Er}^{3+},19\%\text{Yb}^{3+}$ CNP, however, clear increase in lifetime recorded at green emission (corresponding to ${}^2\text{H}_{11/2}$ and ${}^4\text{S}_{3/2}$ states) was noted. It matched well with the UC emission spectrum and the calculated slopes for UC green and red emission bands as mentioned above. Such outcomes confirmed the significant influence of NaYF_4 shell layer on the UC energy transfer mechanism appearing in those samples. The schematic model of the energy transfer mechanisms of $\beta\text{-NaYF}_4\text{:2\%Er}^{3+},19\%\text{Yb}^{3+}\text{@NaYF}_4$ CSNP including cross-relaxation processes is presented in Fig. 7f. The excitation wavelength of 975 nm involved in the experiment is matched to the excitation of the sensitizer Yb^{3+} ions from which energy is transferred to Er^{3+} ions. The energy transfer (ET) from Yb^{3+} to Er^{3+} ions marked with a dashed line in the diagram increases the efficiency of population of ${}^4\text{I}_{11/2}$, ${}^4\text{F}_{9/2}$ and ${}^4\text{I}_{7/2}$ levels, which, as can be seen in the diagram, in our co-doped core-shell structure are involved in both 2-photon and 3-photon upconversion processes. The population of ${}^4\text{I}_{11/2}$ level can be followed by two processes, i.e. 1) ${}^4\text{I}_{11/2} \rightarrow {}^4\text{F}_{7/2}$ ESA process, followed by rapid relaxation to ${}^2\text{H}_{11/2}$, ${}^4\text{S}_{3/2}$ and ${}^4\text{F}_{9/2}$ levels, from which the green and red emissions, respectively occur and 2) nonradiative population of the lower ${}^4\text{I}_{13/2}$ level, from which the next upconversion excitation act to the ${}^4\text{F}_{9/2}$ level takes place. The population of the ${}^4\text{F}_{9/2}$ level allows direct radiative transition to the ground ${}^4\text{I}_{15/2}$ state to occur, resulting in the appearance of red emission at 650 nm. However two other events from this state can also supervene, i.e. nonradiative relaxation to ${}^4\text{I}_{9/2}$ and ${}^4\text{I}_{11/2}$ levels or a population of higher lying ${}^4\text{G}_{11/2}$ level. Both the filling of the ${}^4\text{I}_{11/2}$ level followed by excitation to the ${}^4\text{F}_{7/2}$ level, as well as the process of cross-relaxation occurring as a result of the filling of the ${}^4\text{I}_{9/2}$ and ${}^4\text{G}_{11/2}$ levels, lead to subsequent emission transitions thus increasing the efficiency of the observed green emission. What is more, both these processes, i.e. the occurrence of nonradiative relaxation and excitation to the ${}^4\text{G}_{11/2}$ level reduce the population of the ${}^4\text{F}_{9/2}$ level, which explains the lowering of red emission efficiency in favor of green one.

In this work, we have shown that the coating of the CNP by the additional shell layer reduces the efficiency of the surface-related nonradiative quenching processes resulting in the enhancement of the green emission intensity for CSNP in respect to the CNP. Therefore, the core-shell structure in general improved the intensity of bands and thus also extended the decay times, excluding the red emission in the case of $\beta\text{-NaYF}_4\text{:2\%Er}^{3+},19\%\text{Yb}^{3+}\text{@NaYF}_4$ CSNP, however, such a structure weakened the efficiency of energy transfer.

In order to investigate the suitability of $\beta\text{-NaYF}_4\text{:Er}^{3+},\text{Yb}^{3+}\text{@NaYF}_4$ CSNP for optical temperature sensing, the temperature dependence of UC emission spectra under the 976 nm excitation (power density 4.29 W/cm²) at temperatures ranging from 158 to 320 K was measured (Fig. 8a). As can be clearly seen in emission spectra normalized to the intensity of red band which is presented in the Fig. 8a, the intensity of UC green emission of these CSNP increased with increasing temperature. The luminescence intensity ratio (LIR) related to ${}^2\text{H}_{11/2} \rightarrow {}^4\text{I}_{15/2}$ and ${}^4\text{S}_{3/2} \rightarrow {}^4\text{I}_{15/2}$ transitions of two thermally coupled excited states can be derived from Boltzmann equation as follow³⁶:

$$\text{LIR} = \frac{I_H}{I_S} = \frac{g_H A_H h\nu_H}{g_S A_S h\nu_S} \exp\left(-\frac{\Delta E}{kT}\right) = B \exp\left(-\frac{\Delta E}{kT}\right) \quad (8)$$

where, I_H , I_S , g_H , g_S , A_H , A_S , ν_H and ν_S are the integrated emission intensities, degeneracies, spontaneous emission rates and frequencies of the transitions from the ${}^2\text{H}_{11/2}$ (or ${}^4\text{S}_{3/2}$) state to the ground state, respectively; h is Planck's constant; k is Boltzmann constant ($k \sim 0.695035 \text{ cm}^{-1}/\text{K}$); T is the temperature, ΔE is energy gap between the ${}^2\text{H}_{11/2}$ and ${}^4\text{S}_{3/2}$ levels and B is the associated constant of host lattice.

The energy difference between ${}^2\text{H}_{11/2}$ and ${}^4\text{S}_{3/2}$ levels and the associated constant of $\beta\text{-NaYF}_4$ host lattice were determined by fitting the data by exponential function as presented in Fig. 8b. The obtained $\Delta E/k$ and B values for fit were equal to $\sim 813 \text{ cm}^{-1}$ and 14.27 ($r^2 = 0.998$), respectively.

To evaluate the sensor performance to temperature sensing, the relative thermal sensitivity (S_R) of luminescent thermometer has to be determined. Basing on the experimental data of LIR, both the absolute thermal sensitivity (S_A) and the relative thermal sensitivity (S_R) of synthesized $\beta\text{-NaYF}_4\text{:Er}^{3+},\text{Yb}^{3+}\text{@NaYF}_4$ CSNP was calculated by the following equations³⁶:

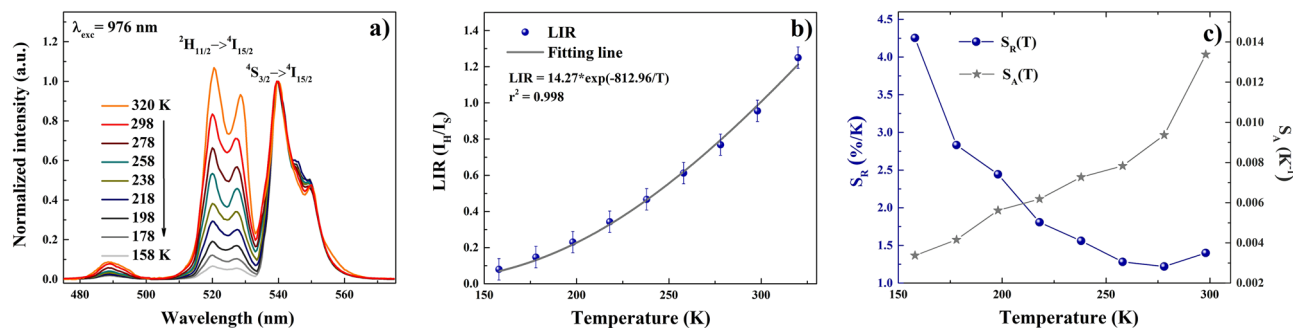


Figure 8. Normalized UC emission spectra of synthesized β -NaYF₄:2%Er³⁺, 19%Yb³⁺@NaYF₄ CSNP upon 976 nm laser diode excitation measured at temperatures ranging from 158 to 320 K with step of 20 K (a), the fluorescence intensity ratio (I_H/I_S) of green emission as a function of temperature where the experimental data is marked as points and the line corresponds to the fitting data (b), the absolute (gray line and stars) and relative (dark blue line and spherical points) sensitivity as a function of temperature (c).

$$S_A = \frac{\Delta(LIR)}{\Delta T} \quad (9)$$

$$S_R = \frac{1}{LIR} \frac{\Delta(LIR)}{\Delta T} \quad (10)$$

The results are presented in the Fig. 8c and as can be seen, the relative thermal sensitivity (dark blue line and spherical points) of β -NaYF₄:Er³⁺, Yb³⁺@NaYF₄ CSNP was decreasing from unprecedented value $S_R = 4.25\% \text{ K}^{-1}$ at 158 K with increasing temperature, however maintaining high value $> 1\% \text{ K}^{-1}$ in the whole analyzed temperature range. On the other hand, the absolute thermal sensitivity (gray line and stars) revealed opposite thermal behavior and increased in this temperature range reaching values of $0.337\% \text{ K}^{-1}$ at 158 K and $1.338\% \text{ K}^{-1}$ at 298 K.

Conclusions

In conclusion, the β -NaYF₄:Er³⁺, Yb³⁺@NaYF₄ CSNP were successfully synthesized by soft template method. The size, shape, crystallinity and UC emission properties of this material were investigated and compared with uncoated β -NaYF₄:Er³⁺, Yb³⁺ CNP. The results obtained shown that the synthesized β -NaYF₄:Er³⁺, Yb³⁺@NaYF₄ CSNP were about 100 ± 10 nm in size, therefore, they were nearly 2.5 times bigger than the β -NaYF₄:Er³⁺, Yb³⁺ CNP. The UC emission spectra measured at room temperature under 976 nm excitation of power density in range from 0.73 to 9.95 W/cm² demonstrated that the synthesized NaYF₄:Er³⁺, Yb³⁺@NaYF₄ CSNP compared with β -NaYF₄:Er³⁺, Yb³⁺ CNP revealed both the stronger UC emission intensity and the 13 times greater the intensity ratio of green to red emission. The calculated CIE (x, y) values have proven the predominance of red color emission in the case of β -NaYF₄:2%Er³⁺, 19%Yb³⁺ CNP and the shift from red color into yellowish green area in the case of NaYF₄:2%Er³⁺, 19%Yb³⁺@NaYF₄ CSNP. The calculated values of slopes of green and red emission intensities versus excitation power density also confirmed that in the NaYF₄:2%Er³⁺, 19%Yb³⁺@NaYF₄ CSNP not only two-photon UC process as in the case of β -NaYF₄:2%Er³⁺, 19%Yb³⁺ CNP occurred, but also three-photon UC process, due to the cross-relaxation existing between Er³⁺ ions took place, enabling green emission intensity enhancement. The calculated lifetimes of ²H_{11/2}, ⁴S_{3/2} and ⁴F_{9/2} excited levels of Er³⁺ ions within single doped β -NaYF₄:2%Er³⁺ CNP and β -NaYF₄@NaYF₄:2%Er³⁺ CSNP were shorter than that of co-doped β -NaYF₄:2%Er³⁺, 19%Yb³⁺ CNP and β -NaYF₄@NaYF₄:2%Er³⁺, 19%Yb³⁺ CSNP, which confirmed that energy transfer from Yb³⁺ to Er³⁺ ions in synthesized materials occurred. What is more, the comparison of β -NaYF₄:2%Er³⁺, 19%Yb³⁺ CNP and β -NaYF₄:2%Er³⁺, 19%Yb³⁺@NaYF₄ CSNP showed that the lifetime of ⁴F_{9/2} excited level associated with red emission band recorded at 650 nm in the case of synthesized core-shell structures was slightly shorter than in uncoated nanoparticles, however, clear increase in lifetime recorded at green emission (corresponding to ²H_{11/2} and ⁴S_{3/2} states) was noted which confirmed the significant influence of NaYF₄ shell on the UC energy transfer mechanisms occurring in core-shell nanomaterials.

The temperature dependent UC emission spectra of β -NaYF₄:2%Er³⁺, 19%Yb³⁺@NaYF₄ CSNPs under the 976 nm laser diode excitation of power density of 4.29 W/cm² have been investigated to evaluate their suitability for temperature sensing applications. Basing on the LIR values of emission bands of two thermally coupled excited states of Er³⁺ ions, the energy gap between ²H_{11/2} and ⁴S_{3/2} levels and associated constant of NaYF₄@NaYF₄ host lattice were determined and they were equal to $\sim 813 \text{ cm}^{-1}$ and 14.27 ($r^2 = 0.998$), respectively. The relative thermal sensitivity of β -NaYF₄:2%Er³⁺, 19%Yb³⁺@NaYF₄ CSNPs determined on the basis of the LIR achieved unusually high value of $S_R = 4.25\% \text{ K}^{-1}$ at 158 K and was decreasing with increasing temperature, however, maintaining value $> 1\% \text{ K}^{-1}$ in the whole analyzed temperature range, up to 298 K. These outcomes confirmed that NaYF₄:2%Er³⁺, 19%Yb³⁺@NaYF₄ CSNPs reveal very high potential for temperature sensing applications.

Received: 18 April 2020; Accepted: 22 June 2020

Published online: 04 September 2020

References

- Childs, P. R. N., Greenwood, J. R. & Long, C. A. Review of temperature measurement. *Rev. Sci. Instrum.* **71**(8), 2959–2978. <https://doi.org/10.1063/1.1305516> (2000).
- Mecklenburg, M. *et al.* Nanoscale temperature mapping in operating microelectronic devices. *Science* **347**, 629–632. <https://doi.org/10.1126/science.aaa2433> (2015).
- Yu, Y. B. & Chow, W. K. Review on an advanced high-temperature measurement technology: the optical fiber thermometry. *J. Thermodyn.* **2009**, 1–11. <https://doi.org/10.1155/2009/823482> (2009).
- Sun, P. S., Sun, M., Tang, Y. Q., Yang, S., Pang, T., Zhang, Z. R. & Dong, F. Z., Measurement of temperature distribution based on optical fiber-sensing technology and tunable diode laser absorption spectroscopy. *Temperature Sensing chapter 3* (Edited by Ivanka Stanimirović, Zdravko Stanimirović, Intech Open, London, United Kingdom) <https://doi.org/10.5772/intechopen.76687> (2018).
- Brites, C. D. S. *et al.* Thermometry at the nanoscale. *Nanoscale* **4**, 4799–4829. <https://doi.org/10.1039/C2NR30663H> (2012).
- Wang, X., Wang, Y., Marques-Hueso, J. & Yan, X. (2017) Improving optical temperature sensing performance of Er³⁺ doped Y₂O₃ microtubes via co-doping and controlling excitation power. *Sci. Rep.* **7**, 758(1–13). <https://doi.org/10.1038/s41598-017-00838-w>.
- Abram, C., Fond, B. & Beyrau, F. Temperature measurement techniques for gas and liquid flows using thermo graphic phosphor tracer particles. *Prog. Energy Combust. Sci.* **64**, 93–156. <https://doi.org/10.1016/j.peecs.2017.09.001> (2018).
- Marciniak, L. & Bednarkiewicz, A. The influence of dopant concentration on temperature dependent emission spectra in LiLa_{1-x}Y_xTb_{0.012} nanocrystals: toward rational design of highly-sensitive luminescent nanothermometers. *Phys. Chem. Chem. Phys.* **18**, 15584–15592. <https://doi.org/10.1039/C6CP00898D> (2016).
- Lu, H. *et al.* Optical sensing of temperature based on non-thermally coupled levels and upconverted white light emission of a Gd₂(WO₄)₃ phosphor co-doped with in Ho(III), Tm(III), and Yb(III). *Microchim. Acta* **184**(2), 641–646. <https://doi.org/10.1007/s00604-016-2070-6> (2017).
- Geitenbeek, R. G., Salzmanna, B. B. V., Nieuwelink, A. E., Meijerink, A. & Weckhuysen, B. M. Chemically and thermally stable lanthanide-doped Y₂O₃ nanoparticles for remote temperature sensing in catalytic environments. *Chem. Eng. Sci.* **198**, 235–240. <https://doi.org/10.1016/j.ces.2018.10.004> (2019).
- Sharma, R. K., Mudring, A. V. & Ghosh, P. Recent trends in binary and ternary rare-earth fluoride nanophosphors: How structural and physical properties influence optical behavior. *J. Lumin.* **189**, 44–63. <https://doi.org/10.1016/j.jlumin.2017.03.062> (2017).
- Tan, M. *et al.* Rare-earth-doped fluoride nanoparticles with engineered long luminescence lifetime for time-gated in vivo optical imaging in the second biological window. *Nanoscale* **10**, 17771–17780. <https://doi.org/10.1039/C8NR02382D> (2018).
- Wang, M., Abbineni, G., Clevenger, A., Mao, C. & Xu, S. Upconversion nanoparticles: synthesis, surface modification, and biological applications. *Nanomedicine* **7**(6), 710–729. <https://doi.org/10.1016/j.nano.2011.02.013> (2011).
- Li, H. *et al.* An upconverting nanotheranostic agent activated by hypoxia combined with NIR irradiation for selective hypoxia imaging and tumour therapy. *J. Mater. Chem. B* **6**, 2747–2757. <https://doi.org/10.1039/C8TB00637G> (2018).
- Peng, Y. P., Lu, W., Ren, P., Ni, Y., Wang, Y., Yan, P., Zeng, Y. J., Zhang, W. & Ruan, S., Multi-band up-converted lasing behavior in NaYF₄:Yb/Er Nanocrystals. *Nanomaterials* **8**, 497 (1–10). <https://doi.org/10.3390/nano8070497> (2018).
- Liu, S. *et al.* pH-sensitive polymerized multifunctional upconversion NaYF₄:Yb/Er@mSiO₂ nanocomposite for oral drug delivery. *Microporous Mesoporous Mater.* **264**, 151–158. <https://doi.org/10.1016/j.micromeso.2018.01.029> (2018).
- Li, Z., Miao, H., Fu, Y., Liu, Y., Zhang, R. and Tang, B., Fabrication of NaYF₄:Yb,Er nanoprobes for cell imaging directly by using the method of hydron rivalry aided by ultrasonic. *Nanoscale Res. Lett.* **11**, 441(1–10). <https://doi.org/10.1186/s11671-016-1651-y> (2016)
- Tang, J., Lei, L., Feng, H., Zhang, H. & Han, Y. Preparation of K⁺-doped core-shell NaYF₄:Yb, Er upconversion nanoparticles and its application for fluorescence immunochromatographic assay of human prolactin. *J. Fluoresc.* **26**(6), 2237–2246. <https://doi.org/10.1007/s10895-016-1919-8> (2016).
- Shota, S., Umezawa, M., Kuraoka, S., Ube, T., Kamimura, M. & Soga, K., Temperature sensing of deep abdominal region in mice by using over-1000 nm near-infrared luminescence of rare-earth-doped NaYF₄ nanothermometer. *Sci. Rep.* **8**, 6979(1–12). <https://doi.org/10.1038/s41598-018-35354-y> (2018)
- Dai, Y. *et al.* Doxorubicin conjugated NaYF₄:Yb³⁺/Tm³⁺ nanoparticles for therapy and sensing of drug delivery by luminescence resonance energy transfer. *Biomaterials* **33**, 8704–8713. <https://doi.org/10.1016/j.biomaterials.2012.08.029> (2012).
- Leipeng, L. *et al.* Study on the thermal sensitivity of β-NaYF₄:Yb³⁺-Er³⁺ nano-thermometers based on luminescence ratiometric technology. *Curr. Appl. Phys.* **19**(4), 480–485. <https://doi.org/10.1016/j.cap.2019.01.021> (2019).
- Wortmann, L., Suyari, S., Ube, T., Kamimura, M. & Soga, K. Tuning the thermal sensitivity of β-NaYF₄: Yb³⁺, Ho³⁺, Er³⁺ nanothermometers for optimal temperature sensing in OTN-NIR (NIR II/III) biological window. *J. Lumin.* **198**, 236–242. <https://doi.org/10.1016/j.jlumin.2018.01.049> (2018).
- Tong, L. *et al.* NaYF₄:Sm³⁺/Yb³⁺@NaYF₄:Er³⁺/Yb³⁺ core-shell structured nanocalorifier with optical temperature probe. *Opt. Express* **25**(14), 16047–16058. <https://doi.org/10.1364/OE.25.016047> (2017).
- Klier, D. T. & Kumke, M. U. Upconversion luminescence properties of NaYF₄:Yb: Er nanoparticles codoped with G^{d3+}. *J. Phys. Chem. C* **119**, 3363–3373. <https://doi.org/10.1021/jp5103548> (2015).
- Geitenbeek, R. G. *et al.* NaYF₄:Er³⁺, Yb³⁺/SiO₂ Core/shell upconverting nanocrystals for luminescence thermometry up to 900 K. *J. Phys. Chem. C* **121**, 3503–3510. <https://doi.org/10.1021/acs.jpcc.6b10279> (2017).
- Li, X., Yang, L., Zhu, Y., Zhong, J. & Chen, D. Upconversion of transparent glass ceramics containing β-NaYF₄:Yb³⁺, Er³⁺ nanocrystals for optical thermometry. *RSC Adv.* **9**, 7948–7954. <https://doi.org/10.1039/C9RA01088B> (2019).
- Cui, Y., Meng, Q., Lü, S. & Sun, W. Temperature sensing properties base on up-conversion luminescence for NaYF₄:Er³⁺, Yb³⁺ phosphor. *Chem. Sel.* **4**, 4316–4323. <https://doi.org/10.1002/slct.201900719> (2019).
- Giang, L. T. K., Anh, T. K., Binh, N. T. & Minh, L. Q. Fabrication and upconversion emission processes in nanoluminophores NaYF₄:Er, Yb and NaYF₄:Tm, Yb. *Int. J. Nanotechnol.* **12**(5), 538–547. <https://doi.org/10.1504/IJNT.2015.067911> (2015).
- Chatterjee, A. K. Chapter 8: X-ray diffraction. In *Handbook of Analytical Techniques in Concrete Science and Technology: Principles, Techniques, and Applications* (Elsevier, 2001). Hardcover ISBN: 9780815514374. <https://doi.org/10.1016/B978-081551437-4.50011-4>.
- Yadav, L. D. S. Chapter 3: Infrared (IR) Spectroscopy. In *Organic Spectroscopy* 52–106 (Springer, Dordrecht, 2005). Print ISBN 978-94-017-2508-8. <https://doi.org/10.1007/978-1-4020-2575-4>.
- Boschetto, F. *et al.* In vitro antibacterial activity of oxide and non-oxide bioceramics for arthroplastic devices: II. Fourier transform infrared spectroscopy. *Analyst* **143**, 2128–2140. <https://doi.org/10.1039/C8AN00234G> (2018).
- Suyver, J. F., Aebischer, A., Garcia-Revilla, S., Gerner, P. & Güdel, H. U., Anomalous power dependence of sensitized upconversion luminescence. *Phys. Rev. B* **71**(12), 125123(1–9). <https://doi.org/10.1103/PhysRevB.71.125123> (2005).
- Xu, S. *et al.* Single-phase white-emitting phosphors Ba₃Ce_(1-x-y)(PO₄)₃:xTb³⁺, yMn²⁺ and B₃Ce_(1-x-z)(PO₄)₃:xTb³⁺, zSm³⁺: structure, luminescence, energy transfer and thermal stability. *RSC Adv.* **7**(32), 19584–19592. <https://doi.org/10.1039/c7ra01766a> (2017).
- Dong, H., Sun, L. D. & Yan, C. H. Energy transfer in lanthanide upconversion studies for extended optical applications. *Chem. Soc. Rev.* **44**(6), 1608–1634. <https://doi.org/10.1039/c4cs00188e> (2015).
- Li, F., Li, J., Chen, L., Huang, Y., Peng, Y., Luo, Y., Zhang, L. & Mu, J., Hydrothermal synthesis and upconversion properties of about 19 nm Sc₂O₃:Er³⁺, Yb³⁺ nanoparticles with detailed investigation of the energy transfer mechanism. *Nanoscale Res. Lett.* **13**, 372(1–9). <https://doi.org/10.1186/s11671-018-2794-9> (2018).

36. Siai, A., Haro-González, P., Horchani Naifer, K. & Férid, M. Optical temperature sensing of Er³⁺/Yb³⁺ doped LaGdO₃ based on fluorescence intensity ratio and lifetime thermometry. *Opt. Mater.* **76**, 34–41. <https://doi.org/10.1016/j.optmat.2017.12.018> (2018).

Acknowledgements

This work is financially supported by *Vietnam National Foundation for Science and Technology Development* (NAFOSTED) under Grant Number 103.03-2016.60.

Author contributions

L.T.K.G. contributed to the research idea, carried out the experiments and wrote manuscript. K.T. and L.M. performed the measurements and revised the manuscript. N.V. and L.Q.M. contributed to helped to research plan and revised manuscript.

Competing interests

The authors declare no competing interests.

Additional information

Correspondence and requests for materials should be addressed to L.T.K.G.

Reprints and permissions information is available at www.nature.com/reprints.

Publisher's note Springer Nature remains neutral with regard to jurisdictional claims in published maps and institutional affiliations.



Open Access This article is licensed under a Creative Commons Attribution 4.0 International License, which permits use, sharing, adaptation, distribution and reproduction in any medium or format, as long as you give appropriate credit to the original author(s) and the source, provide a link to the Creative Commons licence, and indicate if changes were made. The images or other third party material in this article are included in the article's Creative Commons licence, unless indicated otherwise in a credit line to the material. If material is not included in the article's Creative Commons licence and your intended use is not permitted by statutory regulation or exceeds the permitted use, you will need to obtain permission directly from the copyright holder. To view a copy of this licence, visit <http://creativecommons.org/licenses/by/4.0/>.

© The Author(s) 2020